

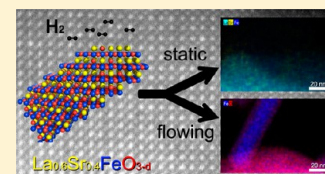
Exsolution of Fe and SrO Nanorods and Nanoparticles from Lanthanum Strontium Ferrite $\text{La}_{0.6}\text{Sr}_{0.4}\text{FeO}_{3-\delta}$ Materials by Hydrogen Reduction

Ramona Thalinger,[†] Martin Gocyla,[‡] Marc Heggen,[‡] Bernhard Klötzer,[†] and Simon Penner^{*,†}

[†]Institute of Physical Chemistry, University of Innsbruck, Innrain 80-82, A-6020 Innsbruck, Austria

[‡]Ernst Ruska Zentrum und Peter Grünberg Institut, Forschungszentrum Jülich GmbH, 52425 Jülich, Germany

ABSTRACT: Formation of uniform Fe and SrO rods as well as nanoparticles following controlled reduction of $\text{La}_{0.6}\text{Sr}_{0.4}\text{FeO}_{3-\delta}$ (LSF) and Ni-LSF samples in dry and moist hydrogen is studied by aberration-corrected electron microscopy. Metallic Fe and SrO precipitate from the perovskite lattice as rods of several tenths of nm and thicknesses up to 20 nm. Based on a model of Fe whisker growth following reduction of pure iron oxides, Fe rod exsolution from LSF proceeds via rate-limiting lattice oxygen removal. This favors the formation of single iron metal nuclei at the perovskite surface, subsequently growing as isolated rods. The latter is only possible upon efficient removal of reduction-induced water and, subsequently, reduction of Fe +III/+IV to Fe(0). If water remains in the system, no reduction or rod formation occurs. In contrast, formation of SrO rods following reduction in dry hydrogen is a catalytic process aided by Ni particles. It bears significant resemblance to surface diffusion-controlled carbon whisker growth on Ni, leading to similar extrusion rods and filaments. In addition to SrO rod growth, the exsolution of Fe nanoparticles and, subsequently, Ni–Fe alloy particles is observed. The latter have also been observed under static hydrogen reduction. Under strict control of the experimental parameters, the presented data therefore open an attractive chemically driven pathway to metal nanoarchitectures beyond the formation of “simple” nanoparticles.



1. INTRODUCTION

In a wide range of research fields, including heterogeneous catalysis, photocatalysis, or energy conversion, tailored functional materials play an ever increasing role.¹ In most cases, this involves nanoparticles dispersed on a variety of structurally different supports, prepared via typical physical or chemical vapor deposition techniques. For electrocatalytically active perovskite materials, recent studies indicate a very elegant pathway of generating well dispersed catalytically active 3D metal nanoparticles, or structures by efficient control of perovskite oxygen anion nonstoichiometry.¹ Exsolution of metal particles from various perovskites such as $\text{La}_{0.6}\text{Sr}_{0.4}\text{FeO}_{3-\delta}$ (LSF)² or $\text{La}_{0.3}\text{Sr}_{0.7}\text{Fe}_{0.7}\text{Cr}_{0.3}\text{O}_{3-\delta}$ ³ is a well-documented phenomenon and has been shown to have significant impact on the physicochemical properties of the materials under question. However, only by controlling the intrinsic material properties (nonstoichiometry or dopants)¹ or extrinsic experimental parameters (oxygen partial pressure, reduction conditions, gas atmosphere),^{3–6} a well-defined system of dispersed nanoparticles can be obtained *in situ*. Of special importance in electrocatalysis is the precipitation, segregation, and exsolution of iron from iron-rich perovskite materials, occurring under sufficiently reducing conditions.^{3–6} In most cases, reversible antisegregation is again observed upon reoxidation, e.g., as outlined in ref 3. For LSF, this iron metal segregation, already induced by mild reductive cathodic polarization in a $\text{H}_2/\text{H}_2\text{O}$ mixture, has been shown to lead to strongly enhanced electrochemical water-splitting kinetics.² Also in this case, subsequent anodic polarization leads to full reversal of the phenomenon. However, despite the important

observations, key structural and morphological features of Fe(0) segregation remained unclear: the presence of Fe(0) was derived from corresponding near-ambient X-ray photoelectron spectroscopy data, which showed a strong Fe(0) contribution in Fe 2p peaks and, in parallel, a strong decrease in total iron intensity during cathodic polarization. This observation was in turn linked to the formation of Fe(0) nanoparticles or, more generally, of 3D nanostructures of Fe(0) exceeding the inelastic mean free path of the photoelectrons. A model picture of this type can in principle explain the observed decrease of XPS-accessible Fe area via exsolution of Fe from near-surface regions.² Of equal importance of the understanding of exsolution phenomena in LSF perovskites are those occurring on technologically more important materials. It is well-known that pure perovskites are promising anode materials in solid-oxide fuel cells, but their catalytic performance can eventually be significantly improved by the addition of catalytically active metals.⁷ The latter, e.g., would include small attached Ni particles for improved methanation reaction performance.⁸ However, this has some significant strings attached, which are connected with high-temperature treatment in hydrogen and the associated stability issues and complex structural segregation behavior. Hydrogen treatment is usually necessary to enter the catalytically active metallic Ni state, and, of equal importance, hydrogen is a reactant in methanation reaction mixtures (e.g., CO or CO_2 and H_2) and product of methane

Received: June 23, 2015

Revised: September 8, 2015

Published: September 9, 2015

reforming.⁸ Possible effects might include, but are not limited to, exsolution of solid iron nanoparticles or Ni–Fe alloy formation. As the exsolution of iron nanoparticles occurs also on the Ni-free Fe-containing perovskites under distinct reduction conditions, the addition of Ni particles, due to dissociative activation of hydrogen, might offer different pathways of perovskite reduction and the subsequent favored exsolution of other elements such as La or Sr in eventually different morphologies.

In the present study, we provide direct electron microscopic insights into the chemically driven exsolution of different metallic and oxidic species of distinct morphology at the atomic level, following controlled reduction treatments of pure LSF and Ni–LSF materials. This involves treatments in hydrogen reaction mixtures of different reduction potentials to narrow the possible decomposition pathways of the perovskite materials. Eventually, the obtained results will, on the one hand, possibly offer an explanation for the so far unknown Fe(0) morphology and the associated XPS intensity effects following cathodic polarization of pure LSF (under comparable reduction conditions);² on the other hand, especially the experiments on Ni–LSF will set the stage for an improved understanding of the structural complexity of those materials, especially under reducing conditions, and its possible influence on catalytic performance.

2. EXPERIMENTAL SECTION

To induce the formation of Fe(0), commercial LSF powder (Sigma-Aldrich, powder <0.5 μm particle size) was treated either in flowing (dry) or static (moist) hydrogen at a temperature of 600 °C. The treatment in dry H_2 at 600 °C exceeds the thermodynamic stability limit of LSF, therefore facilitating the precipitation of Fe(0). Static reduction was performed in a home-built quartz reactor setup including furnace (13 mL volume; about 150 mg sample mass) by treatment in moist hydrogen at 600 °C (1 h, corresponding to a saturation pressure at 300 K of 24 mbar water, 1 bar H_2). Corresponding “dry” treatments were conducted in a comparable quartz reactor setup in flowing hydrogen using a Linn furnace (FRV-25/150/1100) for heating (1 mL s^{-1} , sample mass about 150 mg). Ni–LSF samples were prepared by a standard impregnation technique using Ni acetylacetonate ($\text{Ni}(\text{acac})_2$) as precursor material. The latter was necessary to avoid aquatic impregnation, which might lead to destruction of the perovskite lattice by hydrolysis of alkaline oxides (La_2O_3 , SrO). In detail, $\text{Ni}(\text{acac})_2$ was dissolved in acetone, and the resulting solution poured over the LSF powder. The latter solution was subsequently stirred for 30 min. As a last step, the powder was dried at 100 °C for 1 h and calcined at 600 °C in pure oxygen for 2 h.

Aberration-corrected transmission electron microscopes (FEI Titan 80-300 and TEM Titan 80-300 STEM) and operated 300 kV, as well as a FEI Tecnai G2 F20 operated at 200 kV, were used for imaging. EDX maps were acquired using a FEI Titan 80-200 ChemiSTEM with four Super-X silicon drift detectors, operated at 200 kV.

3. RESULTS

3.1. Pure Perovskite Samples. The structure of the pure LSF sample treated under flowing conditions (1 mL s^{-1}) is shown in Figure 1. All TEM images exhibit rod-like Fe features of different length up to 100 nm and more or less uniform

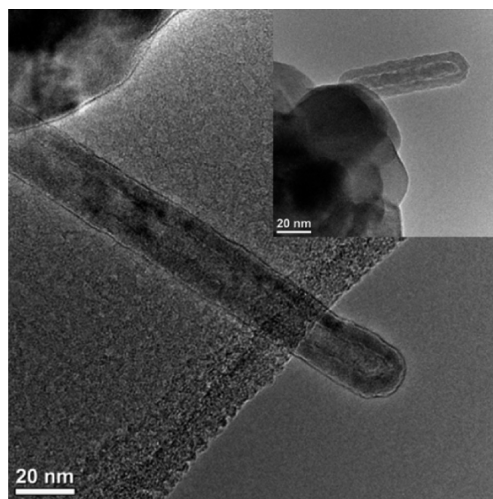


Figure 1. Transmission electron micrographs of LSF after reduction in flowing hydrogen at 600 °C (1 h), highlighting the rod-like morphology of exsolved iron (main panel and inset).

thickness of ~ 20 nm. All rods exhibit some specific internal contrast along the rod contours, appearing as a “shell” surrounding the particle cores. The thickness of these shells is in the range of a few nanometers.

Chemical analysis of the rods is outlined in Figure 2. The basis of this analysis is EDX mapping using the specific electronic transitions of individual elements: energy region Fe–L (blue), O–K (red), Sr–L (yellow), and La–M (turquoise). In subpanels A1–A4, the same rod colored with different elements is shown. It is immediately clear, that the rods almost entirely consist of iron (subpanel A1/2). Oxygen is found within the perovskite bulk (A2), but also appears enriched at the rod edges. This indicates partial oxidation of originally metallic iron in air during transport to the electron microscope. Most importantly, neither strontium (A1) nor lanthanum (A4) is detected within the rods. As EDX mapping indicates some variation of the oxidation state of iron within the rods, the detailed chemical state of iron is further highlighted in panels B and C. EEL spectra (left side of panel B) were taken along the rod axis perpendicular to the perovskite surface, following the color-coded spots shown in panel C. The color code indicates the respective EEL spectra and thus the exact spot, where the spectrum was taken. While the La $M_{4,5}$ intensity (and also the ratio of the M_4 and M_5 peaks) does not change within the perovskite, the Fe $L_{2,3}$ peak shows considerable changes from the rod edge toward its center. In fact, the intensity ratio of the Fe $L_{3/2}$ peaks can be used as an indicator of the Fe oxidation state. High ratios (5–7) indicate Fe in higher oxidation states (+II–+IV); low ratios (4 and below) reduced/metallic Fe.^{9,10} The Fe $L_{3/2}$ peak ratio along the profile is therefore highlighted in the right side of panel B. Oxidized iron is thus only found at the particle edges (and within the perovskite bulk), metallic iron in the rod center. Note that this can be also indirectly derived from the internal HAADF contrast of the iron rod: as the HAADF intensity is mostly dominated by the average atom number, oxygen-rich areas are darker than iron-rich ones, and in turn, the oxygen concentration is highest along the rod edge.

The presence of metallic and oxidized iron is further corroborated by high-resolution imaging (Figure 3). Three images of representative rod areas are shown in panels A (rod

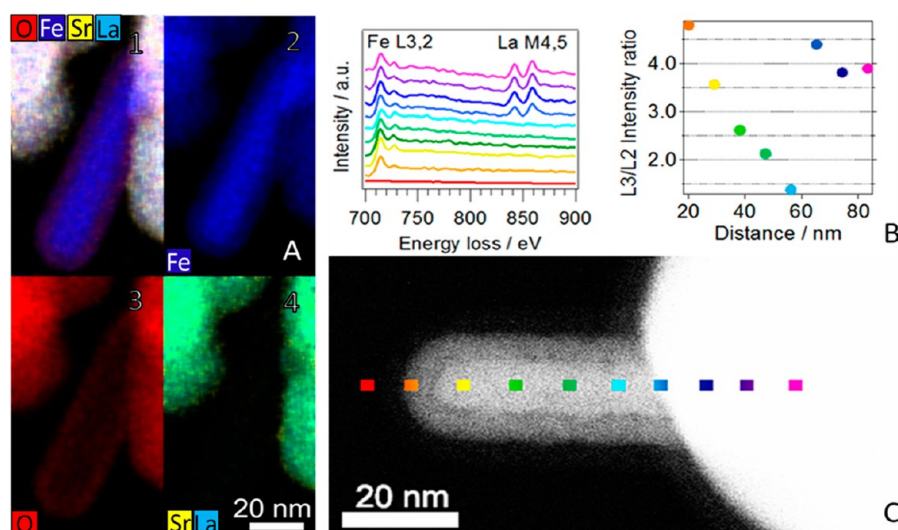


Figure 2. EDX maps using the O–K, Fe–L, Sr–L, and La–M edges to highlight the spatial distribution of the individual elements (A). The chemical state of iron within the rod is highlighted in panel B (individual EEL spectra taken along the spot profile shown in panel C as well as the Fe L_3/L_2 intensity ratio) and panel C (EELS spot profile perpendicular to the LSF surface parallel to the rod). The color code indicates the spot where the respective spectrum was taken.

tip), B (rod center), and C (intergrowth area of LSF grain and rod). From these images, a high crystallinity of the rods can be deduced. To improve the visibility, fast Fourier transforms have been created, and individual colored spots, unambiguously attributable to iron in different oxidation states and LSF, have been used to color-code the corresponding lattice fringes in the HRTEM images. Thus, metallic iron is found mainly in the center, whereas the tip of the rod consists of Fe_3O_4 .^{11–13} Note that magnetite is the only iron oxide that is found in substantial amounts within the rods. Most interesting, with respect to a possible mechanism of iron exsolution, is the atom-resolved intergrowth area of LSF and exsolved Fe rod, shown in panel C. Here, two LSF grains in the upper left and right center region of the image are easily seen; the former has its (006)/(202) lattice spacings color-coded in blue. As these two lattice fringes do not overlap with one of those of Fe_3O_4 , the boundary region of LSF and oxidized Fe rod can be particularly well distinguished.^{11–13} Although one has to take into account the two-dimensional projection of the structure in TEM images, it appears that the upper LSF grain is the origin of the Fe rod and the interface and that the latter is not in highly dynamic state: interdiffusion phenomena or structural defects are largely absent.

To restrict the experimental parameter space that leads to iron rod formation, connecting experiments under static reduction conditions, i.e., at a strongly increased water partial pressure of ~ 24 mbar, have additionally been performed. Figure 4 in turn shows a representative overview TEM image of LSF treated under static conditions. Without exception, the images show agglomerated LSF grains of varying contrast, probably due to thickness variations, but exsolved iron particles or rod-like features have never been observed following this treatment.

Corroborating these findings, Figure 5A in turn shows that indeed no iron segregation or rod formation is observable after this static treatment under otherwise identical experimental conditions (upper panel). The EEL spectra collected along the line shown in Figure 5 (lower panel) do not show any changes. Furthermore, atom-resolved HAADF images (panel B) only

show the terminating Sr–O perovskite surface,¹⁴ but no iron segregation.

In summary, the comparison of harsh (dry hydrogen; flowing) and comparably mild reduction conditions (moist hydrogen; static) already indicate a variable pathway of cation exsolution from the LSF lattice. Before focusing in detail on the exact mechanism, we note the data provide a possible structural explanation for the spectroscopic fingerprint of Fe 2p intensity trends in near-ambient X-ray photoelectron spectra (which were already raised in the Introduction section).² As studies on LSF model electrodes showed enhanced electrochemical water-splitting kinetics following cathodic polarization in humid reducing H_2 atmospheres (i.e., under reducing cathodic conditions) and the associated appearance of Fe(0) in XP spectra, the question was raised on the exact iron morphology formed during reduction.² This was deemed especially important since following cathodic polarization, a strong decrease of the total iron intensity was observed, which could be only explained by exsolution of iron and the corresponding suspected formation of isolated iron nanoparticles on the iron-depleted perovskite surface. The presented microscopy results suggest that this could be connected to rod-like features. In this case, the XPS-accessible Fe area would also decrease as observed in the experiment.

3.2. Ni-Perovskite Samples. For a direct comparison of exsolution phenomena, the following Figures 6–8 show the corresponding experiments on the Ni-LSF sample. In Figure 6 (highlighting the state of the material after flowing reduction in hydrogen at 600 °C), both the EDX maps and the bright-field image of a single Ni particle (panel A, lower right corner) reveal that the Ni particle diameters are typically in the range of 50–100 nm (Ni is colored in green). More importantly, also in this case rod-like features are clearly observable (two rods emanating from a single Ni particle can be seen in the bright-field image in panel A, lower right corner). Interestingly, these rods only contain Sr and O. This is derived from the EDX maps (the Sr–L edge is shown colored in yellow, the O–K edge in red) and from the high-resolution image (upper right inset in panel A). The latter directly reveals that the rods are

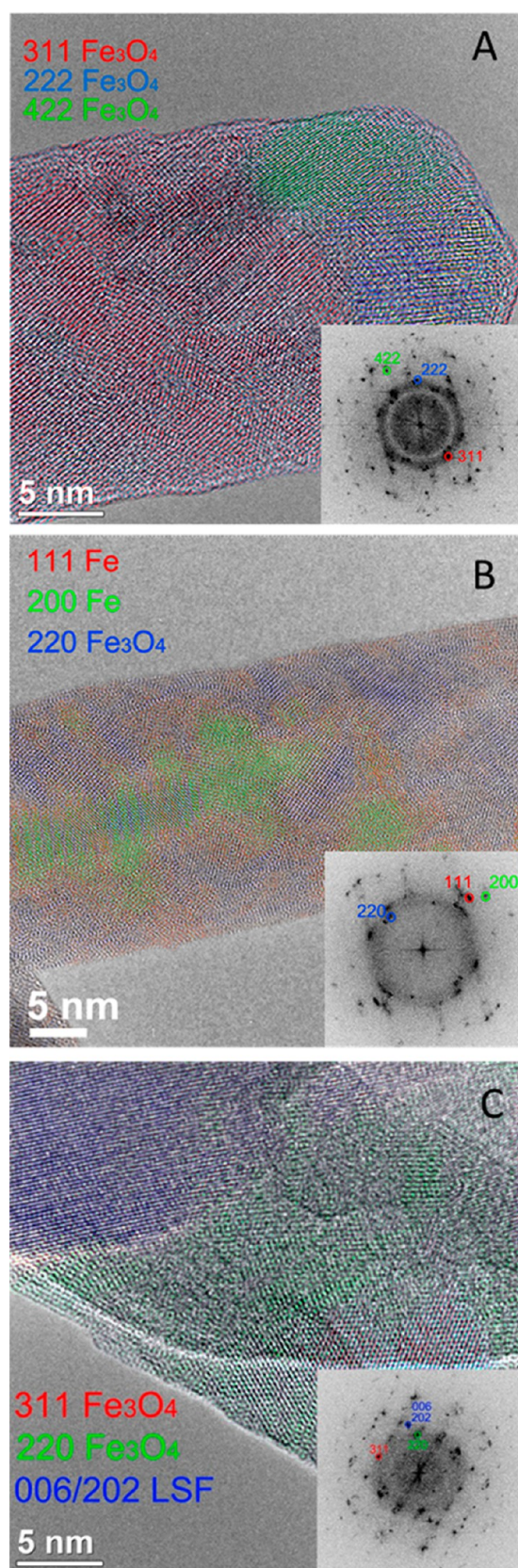


Figure 3. High-resolution TEM images of different areas of a single Fe rod. (A) Rod tip, (B) rod center, and (C) intergrowth area of LSF and Fe rod. For better visibility, selected spots in the fast Fourier transform have been used to color-code specific Fe, Fe_3O_4 , and LSF lattice spacings in the HRTEM image. The upper LSF grain is blue-colored with its 006/202 lattice fringes.

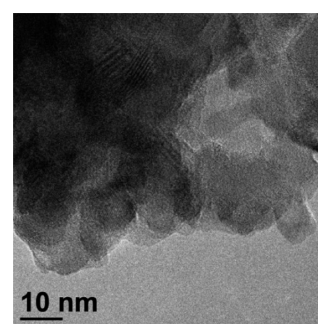


Figure 4. Transmission electron micrographs of LSF after reduction in static hydrogen at 600 °C (1 h).

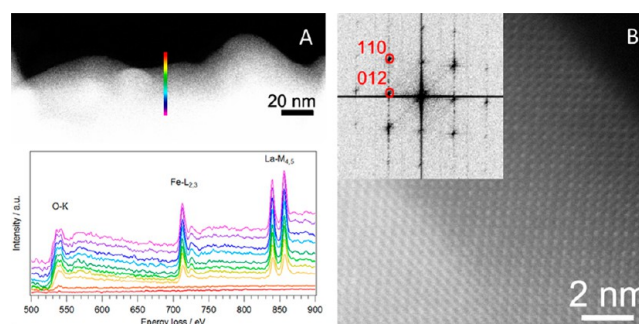


Figure 5. (A) HAADF image of LSF after static reduction in moist hydrogen at 600 °C (1 h, 24 mbar water, 1 bar H_2) with a EELS line profile perpendicular to the surface alongside the corresponding EEL spectra. The color code indicates the spot where the respective spectrum was taken. (B) Corresponding atom-resolved HAADF image of LSF.

composed of crystalline SrO .¹⁹ Note that on Ni-LSF, no Fe-containing rods are observed, although the SrO rod morphology is similar. Rod lengths are in the range of 50 nm, with diameters of about 5 nm. In fact, SrO rod formation is exclusively observed on Ni particles, not directly on LSF grains and also not on additionally exsolved iron nanoparticles. Panel B is particularly interesting because it shows a SrO rod growing partially from a Ni particle (lower image) but also an irregularly shaped SrO particle obviously growing from a LSF grain. This directly reveals that in the present case obviously only Ni can act as growth template for SrO rods. Already at this point, it is clear that perovskite decomposition and exsolution of metal particles takes a different pathway on LSF and Ni-LSF. Predominant SrO exsolution and the importance of Ni is also seen in panel A, revealing the enrichment of $\text{Sr}(\text{O})$ at the LSF-Ni interface as increased bright yellow intensity (marked by black arrows) and SrO covering the accessible Ni area (marked by white arrows).

The subsequent Figures 7 and 8 reveal two exsolution phenomena, which have not been observed on the pure LSF material, but as for pure LSF, under static and flowing reduction conditions strongly depend on the strength of reduction. Flowing reduction yields, as shown in Figure 7, in addition to SrO rod formation, isolated exsolved iron particles, mostly with a pronounced oxide shell around the particle core (oxygen K-edge intensity in red; oxidation most likely happens during transport in air). Under static reduction conditions, iron exsolution is also observed, but single iron particles are very rarely observed. The presence of exsolved iron manifests itself in alloyed Ni-Fe particles, resulting from diffusion of $\text{Fe}(\text{O})$

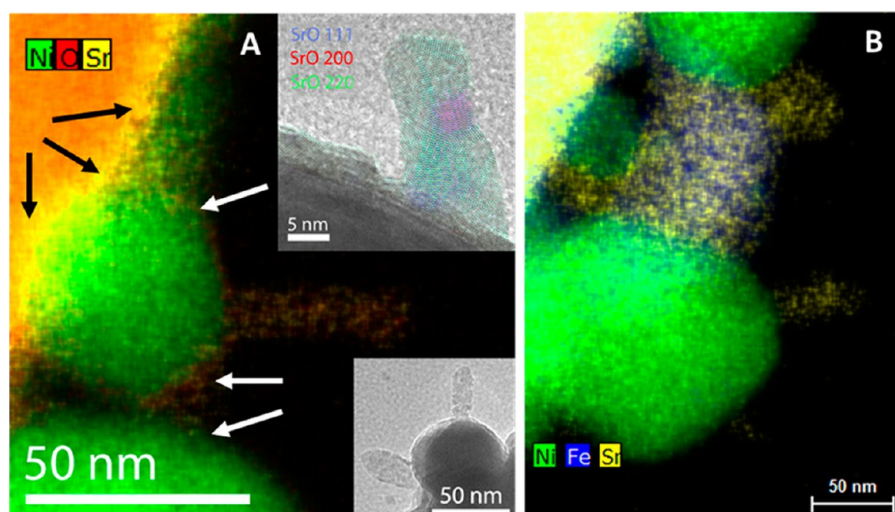


Figure 6. EDX maps using the O–K, Fe–L, Sr–L, and Ni–L intensity to highlight the spatial distribution of the individual elements (after treatment of Ni-LSF in flowing hydrogen at 600 °C (1 h)) (A,B). The insets in panel A shows a high-resolution HRTEM image of a single SrO rod (upper inset) and an overview TEM image of a Ni particle with two attached SrO rods (lower inset). The black and white arrows indicate the enrichment of SrO at the interface and on the Ni surface, respectively.

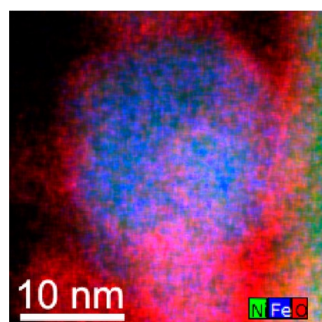


Figure 7. EDX maps using the O–K, Fe–L, and Ni–L edge intensity to highlight the spatial distribution of the individual elements within a single exsolved iron particle with oxidized shell, obtained after treatment of Ni-LSF in flowing hydrogen at 600 °C (1 h).

into the Ni particle. Figure 8 highlights such a particle (panel B), alongside an overview TEM image (panel A). The presence of iron within the particle is usually verified by surface oxidation of iron-rich regions of the alloyed particles. Note that in principle the mere existence of Fe_3O_4 patches on metallic particles could also arise from some kind of strong metal–support interaction effects.²⁰ Such interaction is usually the result of the reduction of an oxidic support in hydrogen at elevated temperatures and leads to loss of active metal area by overgrowth of substoichiometric oxides.²⁰ This has been verified for a number of noble metal particles and a range of oxides, including Fe_3O_4 on Pt particles.²¹ However, in the present case, such structural features of overgrown metal particles are clearly absent.

4. DISCUSSION

Undesired iron whisker formation is a well-documented phenomenon in metallurgical research,^{15–18} which gives valuable hints toward the mechanism of iron exsolution and rod growth also in perovskites: during reduction of iron ore, whisker formation sometimes causes catastrophic swelling of the oxide pellets, leading to disintegration, degradation, and gas permeability changes. Generation of iron metal dust is also

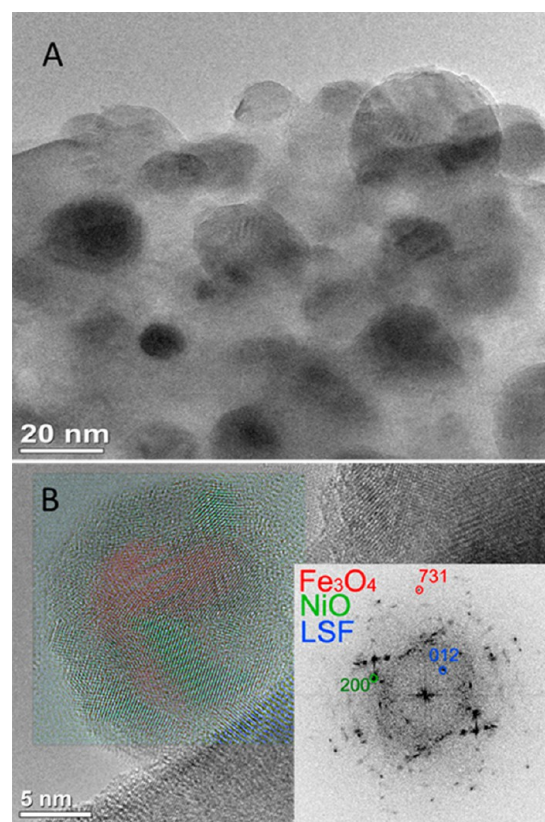
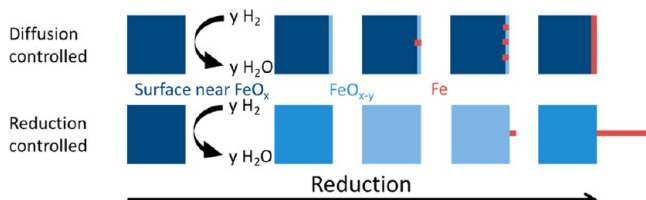


Figure 8. (A) Transmission electron micrographs of Ni-LSF after reduction in static hydrogen at 600 °C (1 h). (B) High-resolution TEM images of different areas of a single alloyed Ni/NiO particle after static reduction in moist hydrogen at 600 °C (1 h, 24 mbar water, 1 bar H_2). For better visibility, selected spots in the fast Fourier transform have been used to color-code specific NiO, LSF, and Fe_3O_4 lattice spacings in the HRTEM image. The square indicates the region where the FFT has been taken.

frequently observed, which bears some resemblance to Ni dusting phenomena in SOFC-related research, causing similar problems of electrode degradation.⁷ Both reduction in CO and

H₂ leads to pellet irregularities and especially during the reduction of FeO (wüstite) to Fe in CO atmosphere, whisker formation is observed. The morphology of the resulting iron metal is subsequently steered by different mechanisms: if iron (cation) transport through the solid is rate determining, this leads to a large density of nuclei, finally merging to a dense layer of iron (Scheme 1, upper panel). Under pure oxygen

Scheme 1. Iron Rod and Layer Formation by Iron-Transport Control (Top) and Oxygen-Removal Control (Bottom)^a



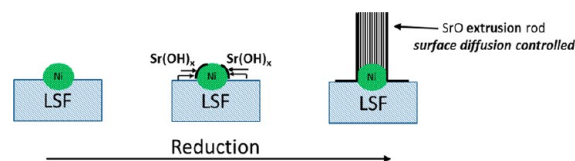
^aMetallic iron is schematically depicted red, reduced iron/perovskite in blue. Dark blue indicates more oxidized, light blue more reduced iron.

(anion) transport control to the surface, iron is reported to be fed down a steep gradient to the nucleus, leaving no time for significant removal of oxygen around the nucleus, leading to outward growth and whisker formation. Under mixed control, conical shapes result.¹⁵ In turn, the documented appearance of rods proves that the reduction of LSF proceeds primarily via “oxygen anion transport control” (Scheme 1, lower panel; dark blue indicates more oxidized, light blue more reduced iron): after creating a supersaturated region with iron beneath the surface and reaching a critical value for nucleation, the first nucleus is formed. Rod formation then takes place only without effective oxygen removal around the nucleus, if the transport of iron from the supersaturated region is much faster than oxygen removal itself. In this case, only one nucleus is formed and acts as a “iron drain”. Oxygen removal therefore is the rate-limiting step and leaves the nucleus no other way than to grow outward. Exactly this situation appears to be fulfilled for LSF under flowing reduction in hydrogen and explains also the situation, why under static conditions no rod formation is observed: reduction is simply too inefficient in terms of oxygen removal.

The question remains to be answered, how the exsolution phenomena observed on the Ni-LSF samples occur mechanistically. In essence, the presence of Ni obviously suppresses the pathway to Fe rods effectively, but opens another pathway to the similar formation of SrO rods (and, additionally, Fe and FeNi nanoparticles). Hence, both Fe and SrO are exsolved simultaneously from the perovskite lattice. In due course, two conclusions can be immediately drawn: First, the absence of Fe rods indicates that the exsolution does not proceed via strict oxygen removal control, but a more complex mechanism must be assumed. Second, the presence of metallic Ni appears to be of even more crucial importance. As Ni is capable of dissociative hydrogen activation, the reduction kinetics around the Ni particles are likely faster; this, as confirmed by the TEM experiments, finally leads to SrO exsolution. Unfortunately, while exsolution of B-site dopants is a common feature in SOFC research and as such, well documented,^{1,3} not only the exact mechanism of Sr/SrO exsolution itself but especially that of SrO rod formation is unclear up to now. One might speculate about a similar mechanism that leads to Fe rod formation: SrO rod formation must therefore also proceed via

strict oxygen removal control; otherwise, continuous SrO layers would be expected, based on the previously discussed model similar to iron whisker formation as iron layer growth on pure LSF. However, as this would corroborate the obvious catalytic action of Ni for SrO rod growth, one might want to stress analogies to the model of catalytic carbon nanowire growth on Ni. In this model, after catalytic decomposition of the carbon fuel, carbon dissolves and diffuses through the Ni particle or on the surface. Subsequently, it precipitates as graphite and nanowires.²² In cases, where bulk diffusion is limited or blocked, nanowire growth controlled by bulk diffusion pushes the Ni particles out, and thus, the Ni particle can then be found at the tip of the nanowire. In some cases, however, this nanoparticle is missing and so-called “extrusion filaments” are formed.²³ This happens, according to a model by Baker and Harris, when surface diffusion is dominating and the catalytic Ni particle is not detached.²⁴ Revisiting Figure 6A again, marked by white arrows, Sr enrichment on the Ni surface is clearly visible. Thus, we might infer that for SrO rod growth, surface diffusion is dominating. A possible mechanism is based on two reasonable assumptions: (i) SrO cannot be reduced to metallic Sr under the chosen reduction conditions and (ii) SrO cannot be dissolved in the Ni particle. The observed SrO rod growth then is the result of a delicate balance between the obvious high interfacial energy of LSF and SrO (derived from the high stability of the SrO termination¹⁴) on the Ni-free perovskite and the obviously dominating cohesive energy of SrO on the Ni particles. This leaves SrO no other choice to grow outward to minimize the energy. The effective transport species might also be related to a hydroxylated Sr(OH)_x species, resulting from dissociative H₂ adsorption on Ni and the subsequent diffusion of H to the Ni-STF interface. Upon transport of these species to Ni, the hydroxy species likely decompose under the chosen reduction conditions and finally lead to SrO rod growth. A schematic picture of the reduction process, leading to a SrO extrusion rod, is depicted in Scheme 2.

Scheme 2. SrO Extrusion Rod Formation by Surface Diffusion Control As Deduced from the EDX Maps and Based on a Corresponding Model of Carbon Extrusion Filament Growth²⁴



5. CONCLUSIONS

Most importantly, the results of this study show how information from quite diametral research areas, such as in the present case, metallurgy, and solid state electrochemistry/fuel cell technology, can be jointly used for improved physicochemical understanding. Although perovskites in general and LSF in particular are important candidates for electrodes in SOFCs and their reduction behavior is well-understood, the structural and application-oriented consequences of deep reduction of these complex oxide systems have so far not been described in detail. Positive or negative consequences possibly arise. In any case, consequences are severe: whisker formation might have beneficial (electro)-

catalytic effects, such as the potential enhancement of water-splitting activity by *in situ* formed Fe(0) “nano-electrodes”, or detrimental structural effects, leading to partial fracture of the LSF structure. Combined studies on pure LSF and Ni-LSF materials directly revealed how this collapse of the LSF structure can give rise to different pathways of metal and oxide exsolution: this includes Fe nanorods without simultaneous Fe nanoparticles (pure LSF, flowing H₂), Ni-Fe alloy particles (Ni-LSF, static H₂), or SrO nanorods and Fe nanoparticles, but no Fe nanorods (Ni-LSF, flowing H₂). Hence, under strict control of the experimental parameters the presented data open an attractive chemically driven pathway to metal and metal oxide nanoarchitectures beyond the formation of “simple” nanoparticles.

Further experimental *in situ* microscopic studies are definitely needed to fully clarify the exact mechanism of whisker formation in complex oxide systems, as so far, information is deduced from chemically similar, but not identical, materials only. This would also include dedicated studies on the exact control of the reduction/cathodic potential in H₂/H₂O mixtures of varying composition to induce or possibly suppress rod formation under water electrolysis conditions.

AUTHOR INFORMATION

Corresponding Author

*E-mail: simon.penner@uibk.ac.at. Tel: +43 512 507 58003.

Notes

The authors declare no competing financial interest.

ACKNOWLEDGMENTS

The work was performed within the platform “Material- and Nanoscience” at the University of Innsbruck. Financial support of the SFB project F45/subproject F45–N16, funded by the Austrian Science Fund, is greatly acknowledged. M.H. gratefully acknowledges financial support by the Deutsche Forschungsgemeinschaft (DFG) through grant HE 7192/1-1. The research leading to these results has received funding from the European Union Seventh Framework Programme under Grant Agreement 312483-ESTEEM2 (Integrated Infrastructure Initiative–I3).

REFERENCES

- (1) Neagu, D.; Tsekouras, G.; Miller, D. N.; Menard, H.; Irvine, J. T. S. In Situ Growth of Nanoparticles Through Control of Non-Stoichiometry. *Nat. Chem.* **2013**, *5*, 916–923 and references therein.
- (2) Opitz, A. K.; Nenning, A.; Rameshan, C.; Rameshan, R.; Blume, R.; Hävecker, M.; Knop-Gericke, A.; Rupprechter, G.; Fleig, J.; Klötzer, B. Enhancing Electrochemical Water-Splitting Kinetics by Polarization-Driven Formation of Near-Surface Iron(0): An In Situ XPS Study on Perovskite-Type Electrodes. *Angew. Chem.* **2015**, *127*, 2666–2670.
- (3) Haag, J. M.; Barnett, S. A.; Richardson, J. W.; Poepelmeier, K. R. Structural and Chemical Evolution of the SOFC Anode La_{0.3}Sr_{0.3}Fe_{0.7}Cr_{0.3}O_{3–δ} Upon Reduction and Oxidation: An In Situ Neutron Diffraction Study. *Chem. Mater.* **2010**, *22*, 3283–3289.
- (4) Qin, Q.; Wu, G.; Chen, S.; Doherty, W.; Xie, K.; Wu, Y. Perovskite Titanate Cathode Decorated by In Situ Grown Iron Nanocatalyst With Enhanced Electrocatalytic Activity For High-Temperature Steam Electrolysis. *Electrochim. Acta* **2014**, *127*, 215–227.
- (5) Oh, T. S.; Gorte, R. J.; Vohs, J. M. Exsolution Behavior of Metal Catalysts From Perovskite Lattice, NAM-24, Extended Abstract O-Tu-403-12, 2015.
- (6) Sun, Y.; Li, J.; Zeng, Y.; Amirkhiz, B. S.; Wang, M.; Behnamian, Y.; Luo, J. A-Site Deficient Perovskite: The Parent For In Situ Exsolution of Highly Active, Regenerable Nano-Particles as SOFC Anodes. *J. Mater. Chem. A* **2015**, *3*, 11048–11056.
- (7) McIntosh, S.; Gorte, R. J. Direct Hydrocarbon Solid Oxide Fuel Cells. *Chem. Rev.* **2004**, *104*, 4845–4865.
- (8) Elliott, D. J.; Lunsford, J. H. Kinetics of the Methanation Reaction over Ru, Ru-Ni, Ru-Cu and Ni Clusters in Zeolite Y. *J. Catal.* **1979**, *57*, 11–26.
- (9) Dennenwaldt, T.; Lübke, M.; Winklhofer, M.; Müller, A.; Döblinger, M.; Sadat Nabi, H.; Gandman, M.; Cohen-Hyams, T.; Kaplan, W.; Moritz, W.; et al. Insights Into the Structural, Electronic, and Magnetic Properties of Fe_{2–x}Ti_xO₃/Fe₂O₃ Thin Films With x = 0.44 Grown on Al₂O₃ (0001). *J. Mater. Sci.* **2015**, *50*, 122–137.
- (10) Gunay, H. B.; Ghods, P.; Isgor, O. B.; Carpenter, G. J. C.; Wu, X. Characterization of Atomic Structure of Oxide Films on Carbon Steel in Simulated Concrete Pore Solutions Using EELS. *Appl. Surf. Sci.* **2013**, *274*, 195–202.
- (11) Basta, E. Z. Some Mineralogical Relationships in the System Fe₂O₃–Fe₃O₄ and the Composition of Titanomagnetite. *Econ. Geol. Bull. Soc. Econ. Geol.* **1959**, *54*, 698–719.
- (12) Malik, S. K.; Joshi, A. G.; Anderson, H. U.; Zhou, X. D.; Xie, Y. X.; Kornecki, M.; Chu, Z.; James, W. J.; Yelon, W. B.; Yang, J.-B. Crystal Structure, Magnetic Properties, and Mössbauer Studies of La_{0.6}Sr_{0.4}FeO_{3–δ} Prepared by Quenching in Different Atmospheres. *Phys. Rev. B: Condens. Matter Mater. Phys.* **2002**, *66*, 184415–184420.
- (13) Haglund, J.; Fernandez-Guillermot, F.; Grimvall, G.; Korling, M. Theory of Bonding in Transition-Metal Carbides and Nitrides. *Phys. Rev. B: Condens. Matter Mater. Phys.* **1993**, *48*, 11685–11891.
- (14) Thalinger, R.; Opitz, A.; Kogler, S.; Heggen, M.; Stroppa, D.; Schmidmair, D.; Fleig, J.; Tappert, R.; Klötzer, B.; Penner, S. Water Gas and Methane Reactivity of Reducible Perovskite-Type Oxides. *J. Phys. Chem. C* **2015**, *119*, 11739–11753.
- (15) Nicolle, R.; Rist, A. The Mechanism of Whisker Growth in the Reduction of Wüstite. *Metall. Trans. B* **1979**, *108*, 429–438.
- (16) Wang, H.; Sohn, H. Y. Effects of Firing and Reduction Conditions on Swelling and Iron Whisker Formation During the Reduction of Iron Oxide Compact. *ISIJ Int.* **2011**, *51*, 906–912.
- (17) Abdel Halim, K. S.; Bahgat, M.; El-Kelesh, H. A.; Nasr, M. I. Metallic Iron Whisker Formation and Growth During Iron Oxide Reduction: Basicity Effect. *Ironmaking Steelmaking* **2009**, *36*, 631–640.
- (18) Bahgat, M.; Halim, K. S. A.; El-Kelesh, H. A.; Nasr, M. I. Metallic Iron Whisker Formation and Growth During Iron Oxide Reduction: K₂O Effect. *Ironmaking Steelmaking* **2009**, *36*, 379–387.
- (19) The Dow Chemical Company Midland, MI; private communication. The Structure of Crystals, 1st Ed., cited in ICDD database 2015, entry number 00-001-0886.
- (20) Tauster, S. J.; Fung, S. C.; Garten, R. L. Strong Metal-Support Interactions. Group 8 Noble Metals Supported on Titanium Dioxide. *J. Am. Chem. Soc.* **1978**, *100*, 170–175.
- (21) Qin, Z.-H.; Lewandowski, M.; Sun, Y.-N.; Shaikhutdinov, S.; Freund, H.-J. Encapsulation of Pt Nanoparticles As A Result of Strong Metal Support Interaction with Fe₃O₄ (111). *J. Phys. Chem. C* **2008**, *112*, 10209–10213.
- (22) de Jong, K.; Geus, J. W. Carbon Nanofibers: Catalytic Synthesis and Applications. *Catal. Rev.: Sci. Eng.* **2000**, *42*, 481–510 and references therein.
- (23) Sinnott, S. B.; Andrews, R.; Qian, D.; Rao, A. M.; Mao, Z.; Dickey, E. C.; Derbyshire, F. Model of Carbon Nanotube Growth Through Chemical Vapor Deposition. *Chem. Phys. Lett.* **1999**, *355*, 25–30.
- (24) Baker, R. T. K.; Waite, R. J. *Formation of Filamentous Carbon in Chemistry and Physics of Carbon 14*; Marcel Dekker: New York, 1978; p 83.